crystals

MDPI

Review

Absorption of Light in Vertical III-V Semiconductor Nanowires for Solar Cell and Photodetector Applications

Nicklas Anttu

Physics, Faculty of Science and Engineering, Åbo Akademi University, FI-20500 Turku, Finland; nicklas.anttu@abo.fi

Abstract: Vertical III-V semiconductor nanowires have shown promising absorption of light for solar cell and photodetector applications. The absorption properties can be tuned through the choice of III-V materials and geometry of the nanowires. Here, we review the recent progress in the design of the absorption properties of both individual nanowires and nanowire arrays. Future directions for the research field are proposed.

Keywords: III-V semiconductor; nanowire; absorption; solar cell; photodetector

1. Introduction

III-V semiconductors (III-Vs) allow for a large tunability for absorption-based applications through the choice of III-Vs used [1]. In the form of nanowires (see Figure 1), the optical response, including the absorption of light, can be further tuned through geometry design [2]. This combination of materials and geometry tuning makes III-V nanowires highly interesting for solar cells and photodetectors [3–8].

In this review, we focus on non-nitride III-Vs, such as InP, GaP, GaAs, InAs, and InSb, and their ternary and quaternary compounds, such as InGaAsP and InAsSb [1]. Nitride III-Vs, such as GaN and InGaN, have found large interest for light-emitting diode (LED) applications [9], but less attention than the non-nitride III-Vs for light-absorption applications, especially in nanowire applications.

Here, the focus is on light spanning approximately 200 nm to 15 µm in wavelength, that is, from ultraviolet (UV) to long-wavelength infrared (IR), including the visible wavelength range of approximately 400 to 700 nm.

Compared to other recent reviews on nanowires for solar cells and photodetectors, e.g., Refs. [3,5,8,10], the present review has an outspoken focus on the underlying optical response.

This review is organized as follows. In Section 2, we discuss the functioning of solar cells and photodetectors, introducing the absorption of light as one of their core properties; in Section 3, a summary of III-Vs is given; in Section 4, we discuss III-V nanowires and their fabrication; in Section 5, we review how absorption in vertical III-V nanowires can be controlled, including examples of realized solar cells and photodetectors; and finally, in Section 6, we discuss future directions for research.

Citation: Anttu, N. Absorption of Light in Vertical III-V Semiconductor Nanowires for Solar Cell and Photodetector Applications. *Crystals* **2023**, *13*, 1292. https://doi.org/10.3390/cryst13091292

Academic Editor: Weijun Ke

Received: 1 August 2023
Revised: 15 August 2023
Accepted: 17 August 2023
Published: 22 August 2023

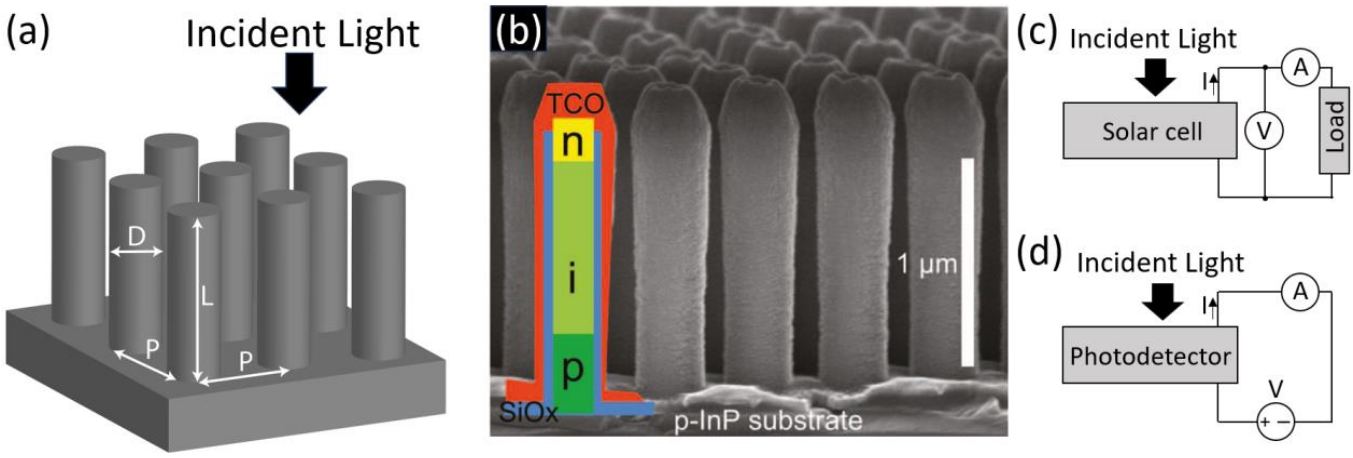

Figure 1. (**a**) Schematic of a nanowire array with nanowires of diameter D and length L in a square array of period P. (**b**) Scanning electron microscopy image of an InP nanowire array solar cell with n, i, and p indicating the regions of the InP diode; TCO indicates the transparent conductive oxide used for the top-side electrical contacting. Reproduced with permission from Ref. [11]. Copyright 2013, the American Association for the Advancement of Science. (**c**) Schematic of a solar cell. The short-circuit current I_{sc} is measured on the ammeter when the resistance of the external load is set to zero, that is, when short-circuiting the external circuit leading to $V = 0$. The short-circuit current (density) j_{sc} is obtained from I_{sc} by normalizing with the active area A_{active} of the solar cell. The open-circuit voltage V_{oc} is measured by removing the external load, that is, by creating an open circuit. In this case, $I = 0$. The output power is given by $P = IV$. By adjusting the external load, it is possible to find the maximum power point P_{mpp} (where we have I_{mpp} and V_{mpp}). The fill-factor FF is defined such that $P_{mpp} = I_{sc}V_{oc}FF$. The efficiency of the solar cell is defined as the maximum fraction of incident power converted to electrical energy, that is, $\eta = j_{sc}V_{oc}FF/\tilde{I}_{inc}$ where $\tilde{I}_{inc}$ is the wavelength-integrated incident solar intensity (which has units of W/m^2). (**d**) Schematic of a photodetector with read-out of electrical current on an ammeter. Here, an external voltage source is used to enhance the signal.

2. Solar Cells and Photodetectors

Solar cells currently contribute to more than 2% of the global electricity production, with an annual 40% growth rate [12]. Photodetectors, on the other hand, are central for a myriad of applications, including high-speed communication technology, imaging, and optical biosensing [13]. Therefore, further progress in either solar cells or photodetectors could have a large impact on our society.

In both solar cells and photodetectors, incident photons are absorbed and converted to an external electrical current [14]. Therefore, the absorption of incident light is a central aspect for the functioning of such optoelectronic devices.

For efficient extraction of photogenerated charge carriers, the electrical design needs to be carefully optimized (see Figure 1b for an example of an axial p-i-n junction in a nanowire, with transparent conductive oxide (TCO) as top contact). However, this review focuses on the absorption of light, and we kindly refer the readers to other works for the electrical design of solar cells and photodetectors [14–19]. We wish, however, to mention that in solar cells, the photogenerated carriers must be extracted with a simultaneous voltage bias created by the solar cell itself, in order to give rise to a net electrical power output from the solar cell [14,15] (see Figure 1c). In contrast, in photodetectors, we can use external power to drive the photodetector, which, for example, allows us to reverse-bias a photodetector diode for more efficient charge extraction, including avalanche photomultiplication to enhance the output electrical (current) signal [14] (see Figure 1d).

2.1. Bandgap of Semiconductors for Absorption Applications

One of the core defining characteristics of a semiconductor is its bandgap E_g [1,14]. The bandgap is the energy separation between the conduction band and the valence band. Absorption of above-bandgap light gives rise to a photogenerated excess electron to the conduction band and an excess hole to the valence band, which can be extracted for electrical output signal [14].

For absorption applications, the bandgap is central in the sense that the absorption strength in the semiconductor rapidly drops for energies below the bandgap energy. The bandgap energy of the semiconductor corresponds to a photon wavelength through the relation $E_g = 2\pi c\hbar/\lambda_g$ where c is the speed of light in vacuum and $\hbar$ is the reduced Planck constant. When expressing the bandgap energy in units of eV and the photon wavelength in units of nm, the relation can be written conveniently as $\lambda_g = 1240/E_g$. Thus, for example in InP with a bandgap of 1.34 eV, the bandgap wavelength is $\lambda_g = 925$ nm, and we expect absorption for photon wavelengths λ shorter than 925 nm. Thus, by choosing the semiconductor material and hence the bandgap, we can affect the onset wavelength for absorption.

2.2. Absorption of Light for Solar Cells and Photodetectors

For solar cells, the incident sunlight spectrum on earth spans approximately from 270 to 4000 nm in wavelength (see Figure 2). With a lower E_g, we can absorb a larger fraction of the incident photons. The short-circuit current can be calculated as $j_{sc} = q\int_0^{\lambda_g} \frac{I_{inc}(\lambda)A_{inc}(\lambda)}{2\pi\hbar c/\lambda} d\lambda$ where q is the elementary charge, $I_{inc}(\lambda)$ is the incident solar spectrum, and $A_{inc}(\lambda)$ is the absorptance, that is, the fraction of incident light that is absorbed (here, it is assumed that each absorbed photon gives rise to one charge carrier to the external current) [18]. See Figure 2 for an example of the maximum obtainable j_{sc} for the case of the $I_{AM1.5D}$ solar spectrum.

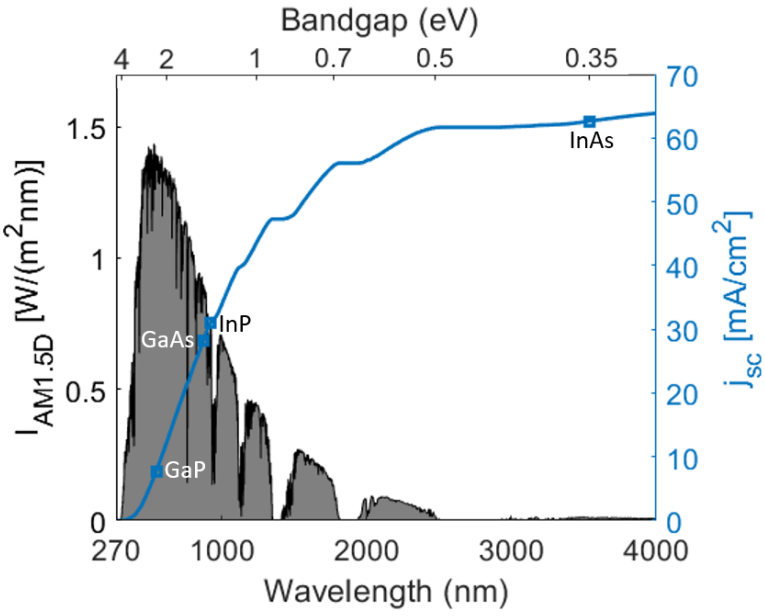

Figure 2. The direct and circumsolar 900 W/m^2 $I_{AM1.5D}$ spectrum (grey patched area) is shown with values on the left axis, with data from Ref. [20]. Here, the corresponding maximum short-circuit current j_{sc} as a function of bandgap wavelength (blue line) is also shown with values on the right axis, under the assumption that all incident above-bandgap photons are absorbed, that is, that $A_{inc}(\lambda) = 1$ for $\lambda < \lambda_g$. The maximum j_{sc} values for the III-Vs listed in Table 1, that is, GaP, GaAs, InP, and InAs, are marked here. The wavelength scale is shown as linear while on the top axis, selected bandgap energies are shown on the resulting non-linear scale.

Table 1. Bandgap, E_g, with values from Ref. [1] at a temperature of 300 K for selected III-V semiconductors. We also show the corresponding bandgap wavelength, λ_g.

III-V	Bandgap (eV)	Bandgap Wavelength (nm)
GaP	2.27 [1]	546
GaAs	1.42	873
InP	1.34	925
InAs	0.35	3540

[1] GaP shows an indirect bandgap with the direct transitions starting at 2.77 eV [1], corresponding to 448 nm in photon wavelength.

However, the bandgap energy also limits the voltage at which a solar cell can operate, as detailed by Shockley and Quiesser in 1961 through a detailed balance analysis [21]. Therefore, there is an optimum E_g in the range of ≈1–1.5 eV for optimizing the electrical power output, and hence, efficiency, of a solar cell based on a single semiconductor material. The current efficiency record of such a single-junction solar cell is at 29.1%, set by a III-V cell [22] based on GaAs with a bandgap of 1.42 eV (however, due to the high manufacturing cost of GaAs solar cells, the solar cell market is dominated by Si solar cells with a record efficiency of 26.8% [22]).

To absorb a larger fraction of the incident photons without sacrificing output voltage, a multi-junction solar cell approach is useful [15]. In this configuration, the solar cell consists of a stack of sub-cells, with the highest bandgap for the sub-cell at the top and decreasing bandgap down into the stack. In this way, each sub-cell absorbs the photons incident on it at a high efficiency, transmitting lower energy photons to the next sub-cell. With this approach, an efficiency of 47.6% has been reached for a III-V-based solar cell, specifically for a [GaInP/GaInAs; GaInAsP/GaInAs] 4-junction solar cell under concentrated sunlight [22].

For photodetector applications, the incident spectrum is not as fixed as for solar cells. Depending on the application, a photodetector might receive a narrow-band or a broad-band incident spectrum. In this review, we aim to cover both cases by looking at the overall absorption-tuning in nanowires.

3. Bandgap and Refractive Index of III-Vs

3.1. Bandgap

We list in Table 1 the bandgaps of some of the binary III-Vs commonly used for absorption applications with nanowires. As can be seen, their λ_g span a wavelength range from 550 nm to 3500 nm, with a continuous tuning if using their ternary or quaternary compounds. With AlGaP or AlGaAs, we could reach $\lambda_g < 550$ nm [1], but the strong oxidation of Al has somewhat limited this research direction for nanowires. InAsSb is an interesting option for even >10 µm photodetection since the ternary shows at a suitable composition a lower bandgap, with $\lambda_g = 12$ µm, than InAs (3.5 µm) or InSb (7.3 µm) [1,23].

3.2. Refractive Index

The optical response of materials is described by their wavelength-dependent and complex-valued refractive index $n(\lambda) = \mathrm{Re}[n(\lambda)] + \mathrm{iIm}[n(\lambda)]$. This $n(\lambda)$ applies for the linear, local, non-magnetic, and time-harmonic response, and together with the Maxwell equations, it theoretically describes the diffraction of light by structured materials, such as thin films and nanowires [24]. For absorption, $\mathrm{Im}[n(\lambda)] > 0$, and as an alternative, we can study the absorption length $L_{\mathrm{abs}}(\lambda) = [4\pi \mathrm{Im}[n(\lambda)]/\lambda]^{-1}$. L_{abs} corresponds to the thickness in a bulk semiconductor over which the intensity of propagating light decays to $1/e \approx 0.37$ due to absorption.

Out of the III-Vs in Table 1, GaP has an indirect bandgap, which leads to weak absorption from $\lambda_g \approx 550$ nm to $\lambda \approx 450$ nm where much stronger, direct optical transitions set in. This is seen as a low value for Im(n) for $450 < \lambda < 550$ nm, with a rapid increase at $\lambda = 450$ nm (Figure 3). For the other III-Vs in Table 1, we find a direct bandgap, and the absorption starts strong directly at λ_g, as evident by the relatively high Im(n) values

there. There is minor absorption also in the Urbach tail at $\lambda > \lambda_g$ due to phonon-assisted absorption, but the strength of this absorption drops rapidly with increasing λ. See the insets in Figure 3 for the corresponding $L_{abs}(\lambda)$ for the III-Vs.

For the III-Vs in Table 1, Re(n) is on the order of 3.5 (Figure 3), as compared to 1 for air and 1.5 for typical oxides and polymers. This comparatively high Re(n), and especially its contrast to the surrounding material, gives rise to strong diffraction and potential for resonant absorption in nanowires [25].

For studying the absorption in nanowires, theoretical modeling can be an efficient approach since it allows a fast and cost-efficient way to vary geometrical and material parameters [24]. Specifically, the linear Maxwell equations with the use of $n(\lambda)$ is an appealing model since the only input that is used is the material choice and the geometry of the nanowire system [24]. We believe that modeled results are highly accurate for describing the optical response of nanowire arrays [24].

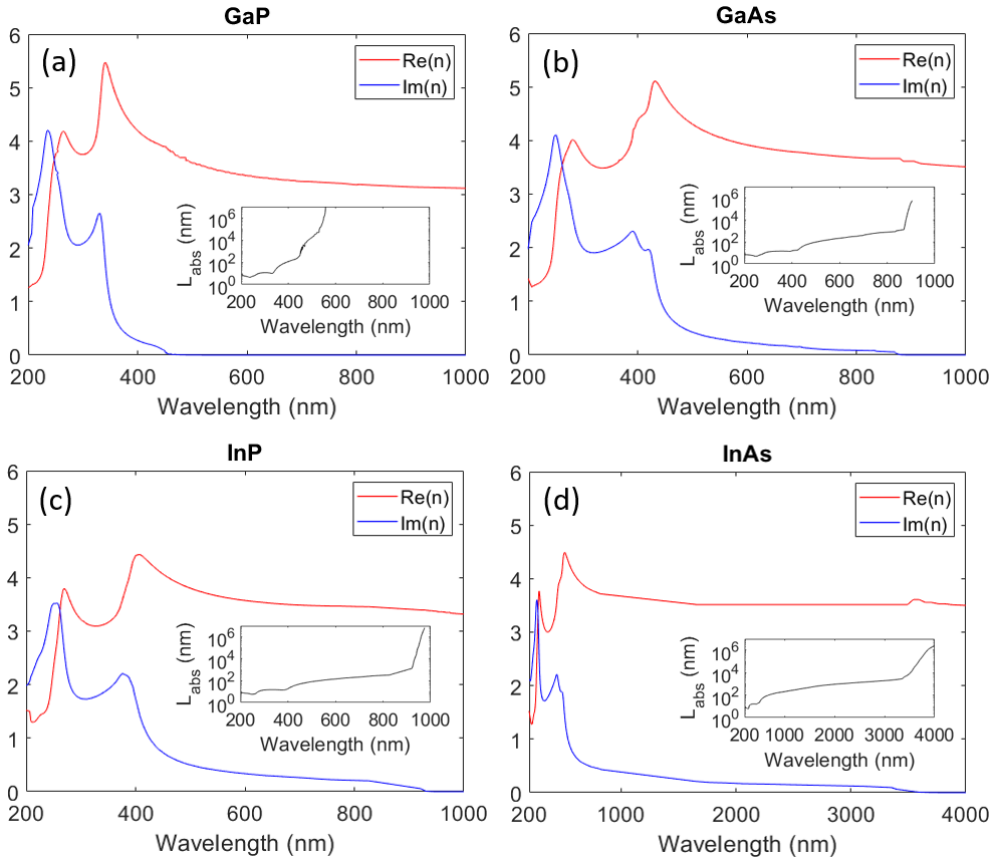

Figure 3. Refractive index of the III-V semiconductors (**a**) GaP, (**b**) GaAs, (**c**) InP, and (**d**) InAs, with tabulated data from Refs. [26–29], respectively. The insets show the corresponding absorption length L_{abs} on a logarithmic scale. Here, we show InAs with an extended wavelength range due to its lower bandgap, see Table 1.

4. III-V Nanowires

As discussed above, III-Vs show large tunability in their optical properties. With III-Vs in nanowire form, we (1) have the prospect of more affordable fabrication [5,10,30,31], (2) gain access to materials combinations otherwise limited by lattice mismatch [32,33], and (3) enable fine tuning of optical responses due to geometry-induced diffraction effects [25].

Nanowires can be fabricated in two main modes: top-down or bottom-up [34]. Properties (1) and (2) above apply for bottom-up fabricated nanowires while property (3) applies also for top-down fabricated nanowires. In top-down fabrication, a planar bulk sample is selectively etched to leave nanowires on the sample. In bottom-up fabrication, nanowires

are synthesized directly into the nanowire form, for example through metal–organic vapor-phase epitaxy (MOVPE) or molecular beam epitaxy (MBE). For both top-down and bottom-up fabrication, the nanowire diameter and length, and possible array pattern, can be controlled to a high degree [34].

When the nanowire diameter is large enough, it is motivated to use the bulk value for $n(\lambda)$ of the nanowire material. For a sufficiently small diameter, quantization effects set in, leading to a diameter-dependent shift in the bandgap energy [35]. A rough guide for when quantization effects set in is the exciton Bohr radius [36], which is given in Ref. [36] as 6 nm for GaP, 15 nm for GaAs, 13 nm for InP, and 57 nm in InAs at a temperature of 300 K. In the case of quantum-well-based nanowire photodetectors [37], due to the quantization in the quantum well, additional considerations for the optical transitions are needed [38]. In the remainder of this review, we assume for simplicity that the diameter and axial extent of the absorbing III-V regions are large enough, such that quantization effects can be ignored when studying the optical response.

5. Tuning of Absorption in Vertical III-V Nanowires

We focus on the case where the absorption in the nanowires is central, that is, we assume that the nanowires contain the electrically active region from which the separation of photogenerated charge carriers occurs in solar cells and photodetectors.

With a III-V nanowire array transferred to a transparent polymer [39,40], it is possible to directly measure the absorption in the nanowires, for example, in an integrating sphere. Such measurements have shown that nanowires can efficiently absorb the light that would pass between them in a ray-optics description [39,40] (see Figures 4 and 5). Furthermore, the reflectance was on the order of a few percentage or less, as compared to a typical reflectance on the order of 30% for a planar III-V sample [39,40].

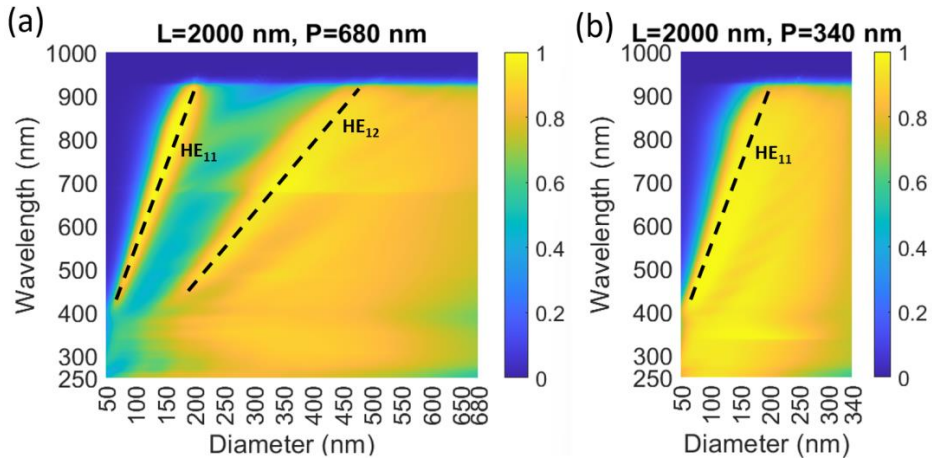

Figure 4. Modeled absorptance of normally incident light in InP nanowires on InP substrate, that is, the same system as studied in Ref. [2], recalculated for this review in the same way as in Ref. [2] to allow this replotting. (**a**) L = 2000 nm and P = 680 nm. For this L, P = 680 nm and D = 441 nm give a peak of $j_{sc} = 27.6$ mA/cm^2, which occurs when the HE_{12} absorption peak is placed in the vicinity of the bandgap wavelength. This P and D is the optimum choice if using the tuning of the HE_{12} absorption peak for this L. (**b**) L = 2000 nm and P = 340 nm. For this L, P = 340 nm and D = 184 nm gives, for any value of D and P, the maximum absorption corresponding to $j_{sc} = 29.0$ mA/cm^2. These values are calculated for the 900 W/m^2 AM1.5D spectrum (see Figure 2) for which the maximum value for InP with $E_g = 1.34$ eV is 31.1 mA/cm^2, which occurs when all above-bandgap light is absorbed (see Figure 2). The horizontal scaling in (**a**) and (**b**) is set to be equal to allow for easier comparison. Here, to guide the eye, we indicate the absorption peak due to the HE_{11} and HE_{12} waveguide modes (dashed lines). The region of low absorptance for small D/λ to the left of the dashed line, which indicates the HE_{11} peak, originates from the electrostatic screening [25]. For InP, $\lambda_g = 925$ nm, and for $\lambda > \lambda_g$, the absorption drops rapidly to negligible values.

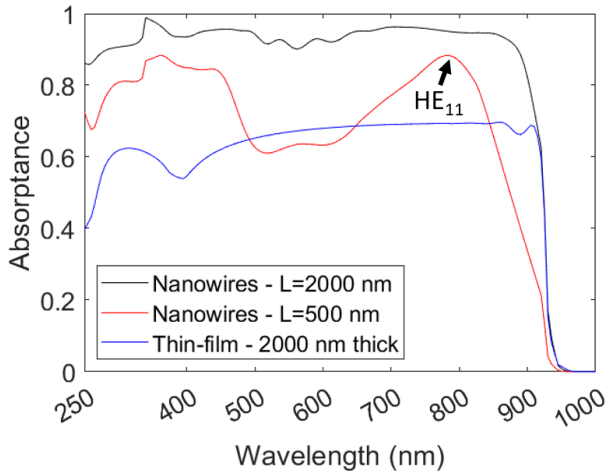

Figure 5. Absorption spectra from Figure 4 for L = 2000 nm, D = 184 nm, and P = 340 nm, which is the optimized D and P for absorbing sunlight for this L. For comparison, we also show here the spectrum for the same D and P but shorter nanowires of L = 500 nm. With this value for D, the absorption peak originating from the HE_{11} waveguide mode (indicated by the arrow) is tuned to the vicinity of the bandgap, and the increase in L saturates absorption for shorter wavelengths. In addition, the absorption spectrum for a thin film of 2000 nm in thickness surrounded by air is shown—the absorption for this thin film is limited by reflection loss, except at $\lambda > 870$ nm where transmission loss starts at 1% and increases toward the bandgap wavelength.

Thus, vertical nanowires can capture light from the surroundings, as also detailed in an early modeling work on Si nanowire arrays [41]. That work focused on small-diameter nanowires. Afterwards, the research field became more and more interested in larger-diameter nanowires where strong diffraction of light can enhance the absorption, for example, by 200-fold per volume absorbing materials in a III-V nanowire array [25].

Note that Si shows $\lambda_g \approx 1100$ nm, but due to the indirect bandgap of Si, Si is rather weakly absorbing in a broad wavelength range [42]. Therefore, results from absorbing Si nanowire arrays are not necessarily directly transferable to direct bandgap III-V nanowires. However, where suitable, we will give reference to related Si nanowire absorption studies below.

5.1. Basic Nanowire Array

The basic nanowire array that we consider is periodic and defined by the nanowire diameter D, nanowire length L, and array period P (see Figure 1a for a schematic). The absorption is typically not strongly dependent on the type of array, with rather similar absorption found for a square and a hexagonal array, as long as the same nanowire density is used for both arrays [18,43]. In the most basic configuration, the nanowires are on a native substrate of the same material as the nanowires and surrounded by air above and between them. In principle, additional processing layers can have noticeable effect on the optical response [18,44], but this basic array functions as a good starting point for more complicated device layouts.

The basic nanowire array has received considerable theoretical interest, and it has been shown that with appropriate geometry choices, the nanowires can absorb incident light very efficiently [2,45–49].

5.1.1. Insertion Reflection Loss

For the above basic nanowire array, a limiting factor for the absorption of light is the insertion reflection loss [2]. This reflection occurs at the top of the nanowire array and depends on D and P, but not on L. Typically, this reflection loss decreases with decreasing D/P ratio, especially if considering averaging over a broadband response, such as the above-bandgap part of the solar spectrum that could be absorbed by the semiconductor [2].

To couple in as much light as possible into the nanowire array for possible absorption, we would like to decrease the D/P ratio. Indeed, with sparse nanowire arrays, it is possible to reach very good broadband incoupling of light [50]. However, with decreasing D/P ratio, the amount of absorbing semiconductor material in the nanowire array decreases. Therefore, it is not surprising that the optimum D/P ratio for absorption is dependent on L. A larger L allows for a smaller D/P ratio for optimized absorption of sunlight [2].

5.1.2. Diameter-Dependent Absorption

The diameter D of the nanowires has a strong impact on the optical response. When $D \gg \lambda$, we are in the geometrical optics regime where light can be described as rays. In this case, for normally incident light, the fraction of light that can be absorbed by the nanowires is limited by the area coverage of the nanowires, that is, the (area) density of nanowires multiplied by the cross-sectional area $\pi D^2/4$ of a nanowire [25]. At the other extreme, when $D \ll \lambda$, we can use an electrostatic description for light. This description reveals a considerably weaker absorption of normally incident light in small-diameter nanowires due to electrostatic screening, as compared to a planar semiconductor layer [25] (see Figures 4 and 5).

In the intermediate regime where $D \approx \lambda$, the nanowires function optically as waveguides, with accompanying electromagnetic waveguide modes [51] (see Figure 6 for a schematic). These waveguide modes depend on the nanowire diameter D, but not on array period P (unless considering a very dense array where nanowire-to-nanowire coupling could affect the dispersion of the waveguide modes [2]).

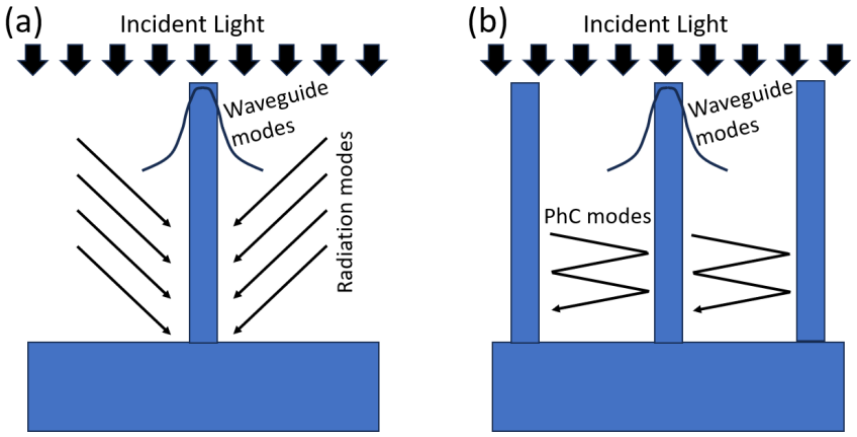

Figure 6. (**a**) Schematic of how light couples into a single nanowire, with the waveguide modes (see Section 5.1.2) and radiation modes (see Section 5.1.4) indicated. (**b**) Schematic of how light couples into a single nanowire, with the waveguide modes (see Section 5.1.2) and photonic crystal modes (see Section 5.1.3) indicated. Note that the waveguide modes in the nanowire array are, strictly speaking, part of the photonic crystal modes. However, when they are strongly bound to a nanowire, they closely resemble the waveguide modes of a single nanowire, making it convenient to distinguish them from other delocalized photonic crystal modes.

In our experience, the waveguide modes show up distinctively in the optical response at least when $L > \lambda/2$. For shorter nanowires, a description based on elongated Mie scatterers might be more suitable [52].

For normally incident light, we find the strongest response from the HE_{1m} waveguide modes [2,53]. The HE_{nm} modes are hybrid modes, with non-zero longitudinal components of both the magnetic (H) and electric (E) field, with n indicating the azimuth dependence of the form $\cos(n\varphi)$ [or $\sin(n\varphi)$] around the nanowire axis and m indicating the radial dependence, with the propagation constant of the mode increasing with increasing m [51]. Each HE_{1m} mode gives rise to a distinct absorption peak whose wavelength position can

be tuned by the nanowire diameter [2,53], as measured initially for the HE_{11} mode in Si nanowire arrays [54].

The absorption peak due to an HE_{1m} mode originates from two factors. First, with increasing D, the waveguide mode becomes more and more bound to the nanowire, which leads to stronger absorption of the light that has coupled into the mode [23,55]. Second, with increasing D, since the waveguide mode becomes more and more bound to the nanowire, it has less and less overlap with the incident plane wave, and less light couples into the mode [23,55]. Therefore, due to these opposite dependencies on D, for an intermediate value for D, we find an absorption peak [23,55].

We note that the waveguide-mode dispersion can be scaled with wavelength, taking into account the variation in Re(n) between semiconductors. Thus, it is not surprising that the HE_{11} mode can be used to give rise to an absorption peak also for longer wavelengths, such as at $\lambda > 3$ μm by scaling the diameter to $D > 500$ nm in InAsSb nanowires [23].

For the broadband absorption of sunlight, it has been found optimal to place the absorption peak due to an HE_{1m} mode in the vicinity of the bandgap wavelength (see Figures 4 and 5). In this way, we enhance the absorption, which is otherwise weak due to the low Im(n) for wavelengths just below the bandgap wavelength. For strongest absorption, it appears that the HE_{11} mode is the most beneficial to use. Therefore, we find a rather constant optimum D for varying nanowire length, while P increases with increasing L, which in turn decreases the D/P ratio and insertion reflection loss as discussed above. Conveniently, if we have found the optimum D for nanowires of one III-V, such as in Ref. [2] for InP nanowires, it is possible to estimate the optimum D for nanowires made of other III-Vs. Thanks to the scalability of the Maxwell equations, to find the optimum diameter for a different III-V, we need to scale with λ_g and the bandgap refractive index values: $D_{m,\mathrm{new}} \approx D_{m,\mathrm{old}} \lambda_{g,\mathrm{new}} n_{\mathrm{old}}\left(\lambda_{g,\mathrm{old}}\right) / \left(\lambda_{g,\mathrm{old}} n_{\mathrm{new}}\left(\lambda_{g,\mathrm{new}}\right)\right)$ [2]. Here, new and old refer to the two different semiconductor materials and m refers to the optimization based on placing the absorption peak from the HE_{1m} mode in the vicinity of the bandgap.

An additional avenue to tune the optical response is to use a dielectric shell on top of the nanowire to increase the effective diameter of the nanowire [56]. Such an approach can be effective for example, if D is too small to reach a desired wavelength with the HE_{11} absorption peak. However, this approach typically does not lead to as strong absorption as when simply increasing the diameter D of the absorbing nanowire itself [56].

5.1.3. Photonic Crystal Modes in Nanowire Arrays

The periodic nanowire array has an enumerable set of discrete optical modes [2,44]. In other words, the nanowire array corresponds to a two-dimensional photonic crystal consisting of cylinders [57]. The electromagnetic field, which describes the light inside the nanowire array, can be described fully in terms of these photonic crystal modes. The photonic crystal modes are excited at the top and the bottom interface of the nanowire array [2].

Thus, when analyzing theoretically the absorption of light in nanowire arrays, it can be powerful to look at the excitation and absorption of the varying photonic crystal modes present, see for example Appendix C in Ref. [2]. For example in the Fourier modal method (FMM) for solving the Maxwell equations for the scattering of light, that modal information is readily available [24,58].

Compared to conventional photonic crystal research, there are, however, some noticeable differences. First, we consider nanowires for absorption applications, in which case, each photonic crystal mode exhibits some degree of absorption, in contrast to typical photonic crystal research with non-absorbing dielectric materials. Second, we consider excitation by external light, where light at a normal angle, that is, parallel to the nanowire axis, corresponds to the Γ point for the photonic crystal. The Γ point for a two-dimensional photonic crystal is typically not of highest interest since due to the continuous translational invariance along the nanowire axis, no photonic bandgap opens up in that direction, since at least one mode is propagating [57] (the HE_{11} mode is the mode that always stays

propagating at the Γ point in the corresponding conventional photonic crystal). Therefore, results from conventional photonic crystal research can have limited applicability for the absorbing nanowire arrays, and dedicated studies about the modal properties in absorbing nanowire arrays are warranted.

5.1.4. Absorption in Single Nanowire vs. Nanowire Array

The HE_{1m} waveguide modes show up in both single nanowires and nanowire arrays, while the photonic crystal modes are exclusive for the nanowire array. For a single nanowire, a continuum of unbound radiation modes shows up instead [55]. Thus, single nanowires also show the HE_{1m}-based absorption peaks, which are tunable by the nanowire diameter [55]. Therefore, a single nanowire shows an optical response strongly set by the HE_{1m} modes. Similar to a nanowire array, (1) the excitation of the HE_{1m} mode can be analyzed based on the overlap of the mode with the incident plane-wave, corresponding to the excitation at the tip of the nanowire, and (2) the absorption along the nanowire axis follows from the imaginary part of the propagation constant of the mode [55].

For long enough nanowires, it is possible to see how the radiation modes couple into the nanowire, leading to additional absorption. Thus, this coupling leads to continued absorption, even after the contribution from the much stronger HE_{1m} absorption has reached a negligible level [55]. Thus, in theory, thanks to coupling from the radiation modes, a single nanowire shows an unbound absorption cross-section with increasing nanowire length [55]. In contrast, a nanowire in a nanowire array shows a limited absorption cross-section due to competition with neighboring nanowires for absorption of incident photons [55].

5.1.5. Dependence on the Incidence Angle

For both solar cells and photodetectors, to maximize the projected area of the device to the incident light, normally incident light is optimum. However, for example, in fixed-installed solar cells, due to the shifting sun position in the sky over the day, varying incidence angles occur. It has been shown that strongly absorbing III-V nanowire arrays remain strongly absorbing to large incidence angles of approximately 60° [59]. However, when considering a single nanowire in detail, it is seen that the optical response becomes incidence angle dependent—at normal incidence, the response is dominated by the HE_{1m} waveguide modes, but with increasing incidence angle, a Mie-type optical response, which is polarization dependent, is found [60].

5.2. Tapered Nanowires

Since the insertion reflection loss in the basic nanowire array decreases with decreasing D/P ratio, it is natural to ask if there is a benefit to using tapered nanowires with increasing diameter further down the nanowire [61] (reduction in reflection and increased light-trapping have been seen also in Si samples with nanocone or nanopyramid texturing [62,63]). Indeed, it has been shown that the absorption in such III-V nanocones can surpass the absorption in corresponding untapered nanowires [64–66]. The tapered geometry also broadens the D-dependent absorption peaks [65,66] by offering a continuum of D-values through the length of the nanowire [67], which is of interest for broadband absorption applications, such as solar cells and broadband photodetectors.

5.3. Aperiodic Arrays

As discussed above, the HE_{1m} absorption peak is diameter dependent. In order to boost absorption in a broader wavelength range, one approach is to use an aperiodic nanowire array where the diameter varies between the nanowires [68,69], as was also proposed for Si nanowires [70,71]. For such aperiodic nanowire arrays, a possible challenge is the formation of the desired pn-junction if fabricated in a bottom-up manner, since the growth and doping conditions might vary nanowire to nanowire.

5.4. Tandem Nanowire-on-Silicon Solar Cells

There is prospect of a low-cost nanowire top cell on top of a high-efficiency Si bottom cell to boost the overall efficiency of the solar cell. Since the bandgap of III-Vs can be fine-tuned by the choice of ternary III-V, such as GaInP, it is possible to find a nanowire top-cell material with an optimized bandgap to be placed on top of a silicon bottom cell. To enable simultaneous strong absorption of above-bandgap photons in the nanowire top cell and efficient transmission of below-bandgap photons to the bottom cell, careful optics considerations are needed, especially if a lower refractive-index spacer is used between the cells [44]. For efficient design, both optical and electrical modeling is needed [19,72].

5.5. Effect of Imperfections in Nanowire Arrays

In large-area nanowire arrays, varying types of imperfections, including missing nanowires and electrical contacting issues of some nanowires are possible [73]. Characterization of such effects then becomes important [73]. In optics simulations, we have seen that neighboring nanowires can efficiently compensate in absorption for a missing nanowire [74]. Thus, missing nanowires appear as a smaller issue than the lack of electrical contacting of a nanowire [74]. In general, the electrical and optical characterization of individual nanowires in processed nanowire arrays are of interest [75].

5.6. Bragg Reflectors in Nanowires

III-V nanowires offer novel ways to create periodic refractive-index variation [76], as needed for example, for Bragg reflectors, that is, dielectric reflectors [77]. In nanowires, it is possible to periodically vary the nanowire diameter in the axial direction [78], an avenue not available in conventional thin-film stacks for Bragg reflectors. We envision the use of Bragg reflectors in nanowires for enhanced absorption of sunlight [79] as well as for wavelength selective and enhanced photodetection.

5.7. Examples of Realized III-V Nanowires Solar Cells and Photodetectors

Research into vertical III-V nanowire solar cells and photodetectors is an active field with multiple studies, e.g., Refs. [11,23,80–97]. Below, we comment on some of them and their connection to the absorption of light (see Table 2 for a summary of the nanowire array solar cells).

Table 2. Summary of the short-circuit current, j_{sc}, open-circuit voltage, V_{oc}, fill-factor, FF, and efficiency, η, of the single-junction III-V nanowire array solar cells referred to in Section 5.7. Note that $\eta = j_{sc}V_{oc}\mathrm{FF}/\widetilde{I}_{inc}$ where $\widetilde{I}_{inc}$ is the wavelength-integrated incident solar intensity [15], which was 1000 W/m^2 for all these devices.

Nanowire Material	j_{sc}	V_{oc}	FF	η	Ref.
InP	24.6	0.779	72.4%	13.8%	[11]
GaAs	21.3	0.906	79.2%	15.3%	[89]
InP	26.6	0.730	77.0%	15.0%	[92]
InP	29.3	0.765	79.4%	17.8%	[90]

In 2013, a 13.8% efficient bottom-up fabricated InP nanowire array solar cell that was 1 mm in size and with 4 million nanowires was realized [11]. The efficiency relied to a large degree on the optimization of the nanowire diameter and pn-junction configuration to enhance charge extraction and j_{sc} [11]. Later, through modeling, it was shown that in such axial pn-junctions, a limiting effect is the extraction of charge carriers from the doped segment closest to the electrical top-side contact [18].

Also in 2013, a solar cell based on a single vertical GaAs nanowire with a short-circuit current density of 180 mA cm^{-2} was demonstrated [83]. This j_{sc} was obtained by normalizing the short-circuit current in the nanowire to the cross-sectional area of the nanowire, and it is approximately 6 times higher than the maximum value in a conventional

GaAs bulk solar cell [22]. Thus, that study clearly shows the excellent possibility for nanowires to capture light from their surroundings.

In 2016, a 15.3% efficient bottom-up fabricated GaAs nanowire array solar cell was reported [89]. For this study, a nanoprobe-contacting scheme inside a scanning electron microscope was used. This electrical contacting allowed electron-beam-induced current measurements, which reveal the spatial variation of charge carrier collection. In 2018, such a nanoprobe contacting and characterization were used for the development of a 15.0% efficient bottom-up fabricated InP nanowire array solar cell [92].

In 2016, a 17.8% efficient top-down fabricated InP nanowire array was shown [90], which currently stands as the record efficiency for III-V nanowire array solar cells. In the initial planar growth, excellent control over the profile for the pn-junction is achieved, leading to a high open-circuit voltage and a high fill-factor. In that study, indium–tin-oxide particles functioned as Mie scatterers to enhance the absorption of light in the top-down etched nanowires.

In 2019, an InP nanowire array photodetector for single-photon detection with a peak efficiency above 90%, without the need of cryogenic cooling, was demonstrated [94]. The excellent optical performance was partly thanks to the tapered design of the nanowires. Two years later, in 2021, a self-powered InP nanowire array photodetector for single-photon detection at room temperature was demonstrated [95].

6. Future Directions

Below, we list some future directions that we find of particular interest for solar cells and photodetectors where they could benefit from nanowires and their unique properties.

For nanowire solar cells, an ongoing and future direction is the epitaxial fabrication of a multi-junction cell into the nanowires themselves, as already demonstrated with GaInP/InP/InAsP triple-junction photovoltaic nanowires [98]. There, a nanowire with GaInP, InP, and InAsP segments in the axial direction was fabricated and characterized. In such a crystalline nanowire, the electrical connection between the varying segments was in the form of an Esaki tunneling diode [98], with external electrical contacting to the top and bottom of the nanowire. We acknowledge this work for simultaneously working around multiple challenges typical for multi-junction nanowires, including the composition control in the two ternary segments, fabrication of the two high-quality tunneling diodes, and fabrication of the pn-junction in each segment. This approach benefits from the freedom in combining materials in the nanowire, despite lattice mismatch. Furthermore, nanowires have been shown to be radiation hard [99], giving the prospect of light-weight and efficient multi-junction nanowire solar cells for space applications. We note that for efficient absorption in the varying segments of such nanowires, some additional geometry design considerations arise compared to the single-junction case [100]. For such solar cell applications, the device size should be scaled up (for example in Ref. [11], a 1 mm by 1 mm large device area was used in 2013). Promising progress has been presented, with growth of nanowires on a 2″ wafer and solar cell devices defined on a 1 cm by 1 cm area in 2023 [73].

Another venue with the nanowires is enabled by embedding them into a flexible host, such as a polymer matrix [39,40]. This gives the prospect for mass-production of flexible solar cells if the nanowires can be successfully contacted electrically and fabricated at a low enough cost. We envision here a flexible, high-efficiency, multi-junction, nanowire solar cell for wearables.

In the above discussion, we have implicitly assumed thermalized carriers in the nanowires. However, in the photogeneration process, hot electrons and hot holes are created in the nanowires due to the excess energy of the absorbed, incident photon. An interesting ongoing and future avenue is the use of hot-carrier effects in nanowire-based solar cells and photodetectors [101]. There, the unique tailoring of the optical and electrical response in nanowires could bring forth benefits beyond planar hot-carrier systems [101].

Funding: This research received no external funding.

Data Availability Statement: No new data were created or analyzed in this study. Data sharing is not applicable to this article.

Conflicts of Interest: The authors declare no conflict of interest.

References

1. Vurgaftman, I.; Meyer, J.R.; Ram-Mohan, L.R. Band Parameters for III–V Compound Semiconductors and Their Alloys. *J. Appl. Phys.* **2001**, *89*, 5815–5875. [CrossRef]
2. Anttu, N.; Xu, H.Q. Efficient Light Management in Vertical Nanowire Arrays for Photovoltaics. *Opt. Express* **2013**, *21*, A558–A575. [CrossRef] [PubMed]
3. Li, Z.; Tan, H.H.; Jagadish, C.; Fu, L. III–V Semiconductor Single Nanowire Solar Cells: A Review. *Adv. Mater. Technol.* **2018**, *3*, 1800005. [CrossRef]
4. VJ, L.; Oh, J.; Nayak, A.P.; Katzenmeyer, A.M.; Gilchrist, K.H.; Grego, S.; Kobayashi, N.P.; Wang, S.-Y.; Talin, A.A.; Dhar, N.K.; et al. A Perspective on Nanowire Photodetectors: Current Status, Future Challenges, and Opportunities. *IEEE J. Sel. Top. Quantum Electron.* **2011**, *17*, 1002–1032. [CrossRef]
5. Otnes, G.; Borgström, M.T. Towards High Efficiency Nanowire Solar Cells. *Nano Today* **2017**, *12*, 31–45. [CrossRef]
6. LaPierre, R.R.; Robson, M.; Azizur-Rahman, K.M.; Kuyanov, P. A Review of III–V Nanowire Infrared Photodetectors and Sensors. *J. Phys. Appl. Phys.* **2017**, *50*, 123001. [CrossRef]
7. LaPierre, R.R.; Chia, A.C.E.; Gibson, S.J.; Haapamaki, C.M.; Boulanger, J.; Yee, R.; Kuyanov, P.; Zhang, J.; Tajik, N.; Jewell, N.; et al. III–V Nanowire Photovoltaics: Review of Design for High Efficiency. *Phys. Status Solidi RRL—Rapid Res. Lett.* **2013**, *7*, 815–830. [CrossRef]
8. Goktas, N.I.; Wilson, P.; Ghukasyan, A.; Wagner, D.; McNamee, S.; LaPierre, R.R. Nanowires for Energy. *Appl. Phys. Rev.* **2018**, *5*, 041305. [CrossRef]
9. Mukai, T. Recent Progress in Group-III Nitride Light-Emitting Diodes. *IEEE J. Sel. Top. Quantum Electron.* **2002**, *8*, 264–270. [CrossRef]
10. Zhang, Y.; Liu, H. Nanowires for High-Efficiency, Low-Cost Solar Photovoltaics. *Crystals* **2019**, *9*, 87. [CrossRef]
11. Wallentin, J.; Anttu, N.; Asoli, D.; Huffman, M.; Åberg, I.; Magnusson, M.H.; Siefer, G.; Fuss-Kailuweit, P.; Dimroth, F.; Witzigmann, B.; et al. InP Nanowire Array Solar Cells Achieving 13.8% Efficiency by Exceeding the Ray Optics Limit. *Science* **2013**, *339*, 1057–1060. [CrossRef]
12. UN Environment Programme. *REN21. Renewables 2022 Global Status Report. (Paris: REN21 Secretariat)*; UN Environment Programme: Gigiri Nairobi, Kenya, 2022; ISBN 978-3-948393-04-5.
13. Downs, C.; Vandervelde, T.E. Progress in Infrared Photodetectors Since 2000. *Sensors* **2013**, *13*, 5054–5098. [CrossRef]
14. Sze, S.M.; Li, Y.; Ng, K.K. *Physics of Semiconductor Devices*; John Wiley & Sons: Hoboken, NJ, USA, 2021; ISBN 978-1-119-61800-3.
15. Nelson, J. *The Physics of Solar Cells*, 1st ed.; ICP: London, UK; River Edge: Singapore, 2003; ISBN 978-1-86094-349-2.
16. Alhalaili, B.; Peksu, E.; Mcphillips, L.N.; Ombaba, M.M.; Islam, M.S.; Karaagac, H. 4 - Nanowires for Photodetection. In *Photodetectors*, 2nd ed.; Nabet, B., Ed.; Woodhead Publishing Series in Electronic and Optical Materials; Woodhead Publishing: Sawston, UK, 2023; pp. 139–197, ISBN 978-0-08-102795-0.
17. Trojnar, A.H.; Valdivia, C.E.; LaPierre, R.R.; Hinzer, K.; Krich, J.J. Optimizations of GaAs Nanowire Solar Cells. *IEEE J. Photovolt.* **2016**, *6*, 1494–1501. [CrossRef]
18. Anttu, N. Physics and Design for 20% and 25% Efficiency Nanowire Array Solar Cells. *Nanotechnology* **2018**, *30*, 074002. [CrossRef] [PubMed]
19. Maryasin, V.; Bucci, D.; Rafhay, Q.; Panicco, F.; Michallon, J.; Kaminski-Cachopo, A. Technological Guidelines for the Design of Tandem III-V Nanowire on Si Solar Cells from Opto-Electrical Simulations. *Sol. Energy Mater. Sol. Cells* **2017**, *172*, 314–323. [CrossRef]
20. *ASTM G173-03(2020)*; Standard Tables for Reference Solar Spectral Irradiances: Direct Normal and Hemispherical on 37° Tilted Surface. ASTM International: West Conshohocken, PA, USA, 2020.
21. Shockley, W.; Queisser, H.J. Detailed Balance Limit of Efficiency of P-n Junction Solar Cells. *J. Appl. Phys.* **1961**, *32*, 510–519. [CrossRef]
22. Green, M.A.; Dunlop, E.D.; Yoshita, M.; Kopidakis, N.; Bothe, K.; Siefer, G.; Hao, X. Solar Cell Efficiency Tables (Version 62). *Prog. Photovolt. Res. Appl.* **2023**, *31*, 651–663. [CrossRef]
23. Svensson, J.; Anttu, N.; Vainorius, N.; Borg, B.M.; Wernersson, L.-E. Diameter-Dependent Photocurrent in InAsSb Nanowire Infrared Photodetectors. *Nano Lett.* **2013**, *13*, 1380–1385. [CrossRef]
24. Anttu, N.; Mäntynen, H.; Sorokina, A.; Turunen, J.; Sadi, T.; Lipsanen, H. Applied Electromagnetic Optics Simulations for Nanophotonics. *J. Appl. Phys.* **2021**, *129*, 131102. [CrossRef]
25. Anttu, N. Geometrical Optics, Electrostatics, and Nanophotonic Resonances in Absorbing Nanowire Arrays. *Opt. Lett.* **2013**, *38*, 730–732. [CrossRef]
26. Borghesi, A.; Guizzetti, G. Gallium Phosphide (GaP). In *Handbook of Optical Constants of Solids*; Palik, E.D., Ed.; Academic Press: Boston, MA, USA, 1985; pp. 445–464, ISBN 978-0-08-054721-3.

27. Palik, E.D. Gallium Arsenide (GaAs). In *Handbook of Optical Constants of Solids*; Palik, E.D., Ed.; Academic Press: Boston, MA, USA, 1985; pp. 429–443, ISBN 978-0-08-054721-3.
28. Glembocki, O.J.; Piller, H. Indium Phosphide (InP). In *Handbook of Optical Constants of Solids*; Palik, E.D., Ed.; Academic Press: Boston, MA, USA, 1997; pp. 503–516, ISBN 978-0-12-544415-6.
29. Pauk, E.D.; Holm, R.T. Indium Arsenide (InAs). In *Handbook of Optical Constants of Solids*; Palik, E.D., Ed.; Academic Press: Boston, MA, USA, 1997; pp. 479–489, ISBN 978-0-12-544415-6.
30. Raj, V.; Haggren, T.; Wong, W.W.; Tan, H.H.; Jagadish, C. Topical Review: Pathways toward Cost-Effective Single-Junction III–V Solar Cells. *J. Phys. Appl. Phys.* **2021**, *55*, 143002. [CrossRef]
31. Barrigón, E.; Hultin, O.; Lindgren, D.; Yadegari, F.; Magnusson, M.H.; Samuelson, L.; Johansson, L.I.M.; Björk, M.T. GaAs Nanowire Pn-Junctions Produced by Low-Cost and High-Throughput Aerotaxy. *Nano Lett.* **2018**, *18*, 1088–1092. [CrossRef]
32. Chuang, L.C.; Moewe, M.; Chase, C.; Kobayashi, N.P.; Chang-Hasnain, C.; Crankshaw, S. Critical Diameter for III-V Nanowires Grown on Lattice-Mismatched Substrates. *Appl. Phys. Lett.* **2007**, *90*, 043115. [CrossRef]
33. Caroff, P.; Messing, M.E.; Borg, B.M.; Dick, K.A.; Deppert, K.; Wernersson, L.-E. InSb Heterostructure Nanowires: MOVPE Growth under Extreme Lattice Mismatch. *Nanotechnology* **2009**, *20*, 495606. [CrossRef] [PubMed]
34. Barrigón, E.; Heurlin, M.; Bi, Z.; Monemar, B.; Samuelson, L. Synthesis and Applications of III–V Nanowires. *Chem. Rev.* **2019**, *119*, 9170–9220. [CrossRef] [PubMed]
35. Loitsch, B.; Rudolph, D.; Morkötter, S.; Döblinger, M.; Grimaldi, G.; Hanschke, L.; Matich, S.; Parzinger, E.; Wurstbauer, U.; Abstreiter, G.; et al. Tunable Quantum Confinement in Ultrathin, Optically Active Semiconductor Nanowires via Reverse-Reaction Growth. *Adv. Mater.* **2015**, *27*, 2195–2202. [CrossRef]
36. Shokhovets, S.; Gobsch, G.; Ambacher, O. Excitonic Contribution to the Optical Absorption in Zinc-Blende III-V Semiconductors. *Phys. Rev. B* **2006**, *74*, 155209. [CrossRef]
37. Erhard, N.; Zenger, S.; Morkötter, S.; Rudolph, D.; Weiss, M.; Krenner, H.J.; Karl, H.; Abstreiter, G.; Finley, J.J.; Koblmüller, G.; et al. Ultrafast Photodetection in the Quantum Wells of Single AlGaAs/GaAs-Based Nanowires. *Nano Lett.* **2015**, *15*, 6869–6874. [CrossRef]
38. Warburton, R.J.; Gauer, C.; Wixforth, A.; Kotthaus, J.P.; Brar, B.; Kroemer, H. Intersubband Resonances in InAs/AlSb Quantum Wells: Selection Rules, Matrix Elements, and the Depolarization Field. *Phys. Rev. B* **1996**, *53*, 7903–7910. [CrossRef]
39. Anttu, N.; Abrand, A.; Asoli, D.; Heurlin, M.; Åberg, I.; Samuelson, L.; Borgström, M. Absorption of Light in InP Nanowire Arrays. *Nano Res.* **2014**, *7*, 816–823. [CrossRef]
40. Hu, S.; Chi, C.-Y.; Fountaine, K.T.; Yao, M.; Atwater, H.A.; Daniel Dapkus, P.; S. Lewis, N.; Zhou, C. Optical, Electrical, and Solar Energy-Conversion Properties of Gallium Arsenide Nanowire -Array Photoanodes. *Energy Environ. Sci.* **2013**, *6*, 1879–1890. [CrossRef]
41. Hu, L.; Chen, G. Analysis of Optical Absorption in Silicon Nanowire Arrays for Photovoltaic Applications. *Nano Lett.* **2007**, *7*, 3249–3252. [CrossRef]
42. Green, M.A. Self-Consistent Optical Parameters of Intrinsic Silicon at 300K Including Temperature Coefficients. *Sol. Energy Mater. Sol. Cells* **2008**, *92*, 1305–1310. [CrossRef]
43. Mariani, G.; Zhou, Z.; Scofield, A.; Huffaker, D.L. Direct-Bandgap Epitaxial Core–Multishell Nanopillar Photovoltaics Featuring Subwavelength Optical Concentrators. *Nano Lett.* **2013**, *13*, 1632–1637. [CrossRef] [PubMed]
44. Dagytė, V.; Anttu, N. Modal Analysis of Resonant and Non-Resonant Optical Response in Semiconductor Nanowire Arrays. *Nanotechnology* **2018**, *30*, 025710. [CrossRef] [PubMed]
45. Kupec, J.; Witzigmann, B. Dispersion, Wave Propagation and Efficiency Analysis of Nanowire Solar Cells. *Opt. Express* **2009**, *17*, 10399–10410. [CrossRef] [PubMed]
46. Guo, H.; Wen, L.; Li, X.; Zhao, Z.; Wang, Y. Analysis of Optical Absorption in GaAs Nanowire Arrays. *Nanoscale Res. Lett.* **2011**, *6* 617. [CrossRef]
47. Wen, L.; Zhao, Z.; Li, X.; Shen, Y.; Guo, H.; Wang, Y. Theoretical Analysis and Modeling of Light Trapping in High Efficicency GaAs Nanowire Array Solar Cells. *Appl. Phys. Lett.* **2011**, *99*, 143116. [CrossRef]
48. Hu, Y.; LaPierre, R.R.; Li, M.; Chen, K.; He, J.-J. Optical Characteristics of GaAs Nanowire Solar Cells. *J. Appl. Phys.* **2012**, *112*, 104311. [CrossRef]
49. Huang, N.; Lin, C.; Povinelli, M.L. Broadband Absorption of Semiconductor Nanowire Arrays for Photovoltaic Applications. *J. Opt.* **2012**, *14*, 024004. [CrossRef]
50. Fountaine, K.T.; Cheng, W.-H.; Bukowsky, C.R.; Atwater, H.A. Near-Unity Unselective Absorption in Sparse InP Nanowire Arrays. *ACS Photonics* **2016**, *3*, 1826–1832. [CrossRef]
51. Snyder, A.W.; Love, J.D. *Optical Waveguide Theory*; Springer: Boston, MA, USA, 1984; ISBN 978-0-412-24250-2.
52. Traviss, D.J.; Schmidt, M.K.; Aizpurua, J.; Muskens, O.L. Antenna Resonances in Low Aspect Ratio Semiconductor Nanowires. *Opt. Express* **2015**, *23*, 22771–22787. [CrossRef] [PubMed]
53. Wang, B.; Leu, P.W. Tunable and Selective Resonant Absorption in Vertical Nanowires. *Opt. Lett.* **2012**, *37*, 3756–3758. [CrossRef] [PubMed]
54. Seo, K.; Wober, M.; Steinvurzel, P.; Schonbrun, E.; Dan, Y.; Ellenbogen, T.; Crozier, K.B. Multicolored Vertical Silicon Nanowires. *Nano Lett.* **2011**, *11*, 1851–1856. [CrossRef]
55. Anttu, N. Absorption of Light in a Single Vertical Nanowire and a Nanowire Array. *Nanotechnology* **2019**, *30*, 104004. [CrossRef]

56. Anttu, N.; Namazi, K.L.; Wu, P.M.; Yang, P.; Xu, H.; Xu, H.Q.; Håkanson, U. Drastically Increased Absorption in Vertical Semiconductor Nanowire Arrays: A Non-Absorbing Dielectric Shell Makes the Difference. *Nano Res.* **2012**, *5*, 863–874. [CrossRef]
57. Joannopoulos, J.D.; Johnson, S.G.; Winn, J.N.; Meade, R.D. *Photonic Crystals: Molding the Flow of Light*, 2nd ed.; Princeton University Press: Princeton, NJ, USA, 2008; ISBN 978-0-691-12456-8.
58. Anttu, N.; Mäntynen, H.; Sadi, T.; Matikainen, A.; Turunen, J.; Lipsanen, H. Comparison of Absorption Simulation in Semiconductor Nanowire and Nanocone Arrays with the Fourier Modal Method, the Finite Element Method, and the Finite-Difference Time-Domain Method. *Nano Express* **2020**, *1*, 030034. [CrossRef]
59. Ghahfarokhi, O.M.; Anttu, N.; Samuelson, L.; Åberg, I. Performance of GaAs Nanowire Array Solar Cells for Varying Incidence Angles. *IEEE J. Photovolt.* **2016**, *6*, 1502–1508. [CrossRef]
60. Abujetas, D.R.; Paniagua-Domínguez, R.; Sánchez-Gil, J.A. Unraveling the Janus Role of Mie Resonances and Leaky/Guided Modes in Semiconductor Nanowire Absorption for Enhanced Light Harvesting. *ACS Photonics* **2015**, *2*, 921–929. [CrossRef]
61. Fan, Z.; Kapadia, R.; Leu, P.W.; Zhang, X.; Chueh, Y.-L.; Takei, K.; Yu, K.; Jamshidi, A.; Rathore, A.A.; Ruebusch, D.J.; et al. Ordered Arrays of Dual-Diameter Nanopillars for Maximized Optical Absorption. *Nano Lett.* **2010**, *10*, 3823–3827. [CrossRef]
62. Cho, Y.; Gwon, M.; Park, H.-H.; Kim, J.; Kim, D.-W. Wafer-Scale Nanoconical Frustum Array Crystalline Silicon Solar Cells: Promising Candidates for Ultrathin Device Applications. *Nanoscale* **2014**, *6*, 9568–9573. [CrossRef] [PubMed]
63. Mavrokefalos, A.; Han, S.E.; Yerci, S.; Branham, M.S.; Chen, G. Efficient Light Trapping in Inverted Nanopyramid Thin Crystalline Silicon Membranes for Solar Cell Applications. *Nano Lett.* **2012**, *12*, 2792–2796. [CrossRef] [PubMed]
64. Diedenhofen, S.L.; Janssen, O.T.A.; Grzela, G.; Bakkers, E.P.A.M.; Gómez Rivas, J. Strong Geometrical Dependence of the Absorption of Light in Arrays of Semiconductor Nanowires. *ACS Nano* **2011**, *5*, 2316–2323. [CrossRef] [PubMed]
65. Wang, B.; Stevens, E.; Leu, P.W. Strong Broadband Absorption in GaAs Nanocone and Nanowire Arrays for Solar Cells. *Opt. Express* **2014**, *22*, A386–A395. [CrossRef] [PubMed]
66. Wilson, D.P.; LaPierre, R.R. Simulation of Optical Absorption in Conical Nanowires. *Opt. Express* **2021**, *29*, 9544–9552. [CrossRef] [PubMed]
67. Tekcan, B.; van Kasteren, B.; Grayli, S.V.; Shen, D.; Tam, M.C.; Ban, D.; Wasilewski, Z.; Tsen, A.W.; Reimer, M.E. Semiconductor Nanowire Metamaterial for Broadband Near-Unity Absorption. *Sci. Rep.* **2022**, *12*, 9663. [CrossRef]
68. Wu, D.; Tang, X.; Wang, K.; Li, X. An Analytic Approach for Optimal Geometrical Design of GaAs Nanowires for Maximal Light Harvesting in Photovoltaic Cells. *Sci. Rep.* **2017**, *7*, 46504. [CrossRef] [PubMed]
69. Yan, X.; Gong, L.; Ai, L.; Wei, W.; Zhang, X.; Ren, X. Enhanced Photovoltaic Performance of Nanowire Array Solar Cells with Multiple Diameters. *Opt. Express* **2018**, *26*, A974–A983. [CrossRef] [PubMed]
70. Lin, C.; Povinelli, M.L. Optimal Design of Aperiodic, Vertical Silicon Nanowire Structures for Photovoltaics. *Opt. Express* **2011**, *19*, A1148–A1154. [CrossRef]
71. Sturmberg, B.C.P.; Dossou, K.B.; Botten, L.C.; Asatryan, A.A.; Poulton, C.G.; McPhedran, R.C.; Sterke, C.M. de Absorption Enhancing Proximity Effects in Aperiodic Nanowire Arrays. *Opt. Express* **2013**, *21*, A964–A969. [CrossRef]
72. Benali, A.; Michallon, J.; Regreny, P.; Drouard, E.; Rojo, P.; Chauvin, N.; Bucci, D.; Fave, A.; Kaminski-Cachopo, A.; Gendry, M. Optical Simulation of Multijunction Solar Cells Based on III-V Nanowires on Silicon. *Energy Procedia* **2014**, *60*, 109–115. [CrossRef]
73. Alcer, D.; Hrachowina, L.; Hessman, D.; Borgström, M.T. Processing and Characterization of Large Area InP Nanowire Photovoltaic Devices. *Nanotechnology* **2023**, *34*, 295402. [CrossRef] [PubMed]
74. Anttu, N. Absorption of Light in Finite Semiconductor Nanowire Arrays and the Effect of Missing Nanowires. *Symmetry* **2021**, *13*, 1654. [CrossRef]
75. Li, Z.; Li, L.; Wang, F.; Xu, L.; Gao, Q.; Alabadla, A.; Peng, K.; Vora, K.; Hattori, H.T.; Hoe Tan, H.; et al. Investigation of Light–Matter Interaction in Single Vertical Nanowires in Ordered Nanowire Arrays. *Nanoscale* **2022**, *14*, 3527–3536. [CrossRef] [PubMed]
76. Grain, N.; Kim, S. Insight into Refractive Index Modulation as Route to Enhanced Light Coupling in Semiconductor Nanowires. *Opt. Lett.* **2023**, *48*, 227–230. [CrossRef] [PubMed]
77. Saleh, B.E.A.; Teich, M.C. *Fundamentals of Photonics*, 2nd ed.; John Wiley and Sons Ltd.: Princeton, NJ, USA, 2007.
78. Wilson, D.P.; LaPierre, R.R. Corrugated Nanowires as Distributed Bragg Reflectors. *Nano Express* **2022**, *3*, 035005. [CrossRef]
79. Aghaeipour, M.; Pettersson, H. Enhanced Broadband Absorption in Nanowire Arrays with Integrated Bragg Reflectors. *Nanophotonics* **2018**, *7*, 819–825. [CrossRef]
80. Czaban, J.A.; Thompson, D.A.; LaPierre, R.R. GaAs Core−Shell Nanowires for Photovoltaic Applications. *Nano Lett.* **2009**, *9*, 148–154. [CrossRef]
81. Colombo, C.; Heiβ, M.; Grätzel, M.; Fontcuberta i Morral, A. Gallium Arsenide P-i-n Radial Structures for Photovoltaic Applications. *Appl. Phys. Lett.* **2009**, *94*, 173108. [CrossRef]
82. Goto, H.; Nosaki, K.; Tomioka, K.; Hara, S.; Hiruma, K.; Motohisa, J.; Fukui, T. Growth of Core–Shell InP Nanowires for Photovoltaic Application by Selective-Area Metal Organic Vapor Phase Epitaxy. *Appl. Phys. Express* **2009**, *2*, 035004. [CrossRef]
83. Krogstrup, P.; Jørgensen, H.I.; Heiss, M.; Demichel, O.; Holm, J.V.; Aagesen, M.; Nygard, J.; Fontcuberta i Morral, A. Single-Nanowire Solar Cells beyond the Shockley–Queisser Limit. *Nat. Photonics* **2013**, *7*, 306–310. [CrossRef]
84. Mariani, G.; Scofield, A.C.; Hung, C.-H.; Huffaker, D.L. GaAs Nanopillar-Array Solar Cells Employing in Situ Surface Passivation. *Nat. Commun.* **2013**, *4*, 1497. [CrossRef] [PubMed]

85. Yao, M.; Huang, N.; Cong, S.; Chi, C.-Y.; Seyedi, M.A.; Lin, Y.-T.; Cao, Y.; Povinelli, M.L.; Dapkus, P.D.; Zhou, C. GaAs Nanowire Array Solar Cells with Axial p–i–n Junctions. *Nano Lett.* **2014**, *14*, 3293–3303. [CrossRef]
86. Cui, Y.; Wang, J.; Plissard, S.R.; Cavalli, A.; Vu, T.T.T.; van Veldhoven, R.P.J.; Gao, L.; Trainor, M.; Verheijen, M.A.; Haverkort, J.E.M.; et al. Efficiency Enhancement of InP Nanowire Solar Cells by Surface Cleaning. *Nano Lett.* **2013**, *13*, 4113–4117. [CrossRef]
87. Yao, M.; Cong, S.; Arab, S.; Huang, N.; Povinelli, M.L.; Cronin, S.B.; Dapkus, P.D.; Zhou, C. Tandem Solar Cells Using GaAs Nanowires on Si: Design, Fabrication, and Observation of Voltage Addition. *Nano Lett.* **2015**, *15*, 7217–7224. [CrossRef] [PubMed]
88. Ko, W.S.; Tran, T.-T.D.; Bhattacharya, I.; Ng, K.W.; Sun, H.; Chang-Hasnain, C. Illumination Angle Insensitive Single Indium Phosphide Tapered Nanopillar Solar Cell. *Nano Lett.* **2015**, *15*, 4961–4967. [CrossRef] [PubMed]
89. Åberg, I.; Vescovi, G.; Asoli, D.; Naseem, U.; Gilboy, J.P.; Sundvall, C.; Dahlgren, A.; Svensson, K.E.; Anttu, N.; Björk, M.T.; et al. A GaAs Nanowire Array Solar Cell with 15.3% Efficiency at 1 Sun. *IEEE J. Photovolt.* **2016**, *6*, 185–190. [CrossRef]
90. van Dam, D.; van Hoof, N.J.J.; Cui, Y.; van Veldhoven, P.J.; Bakkers, E.P.A.M.; Gómez Rivas, J.; Haverkort, J.E.M. High-Efficiency Nanowire Solar Cells with Omnidirectionally Enhanced Absorption Due to Self-Aligned Indium–Tin–Oxide Mie Scatterers. *ACS Nano* **2016**, *10*, 11414–11419. [CrossRef] [PubMed]
91. Sanatinia, R.; Berrier, A.; Dhaka, V.; Perros, A.P.; Huhtio, T.; Lipsanen, H.; Anand, S. Wafer-Scale Self-Organized InP Nanopillars with Controlled Orientation for Photovoltaic Devices. *Nanotechnology* **2015**, *26*, 415304. [CrossRef]
92. Otnes, G.; Barrigón, E.; Sundvall, C.; Svensson, K.E.; Heurlin, M.; Siefer, G.; Samuelson, L.; Åberg, I.; Borgström, M.T. Understanding InP Nanowire Array Solar Cell Performance by Nanoprobe-Enabled Single Nanowire Measurements. *Nano Lett.* **2018**, *18*, 3038–3046. [CrossRef]
93. Mukherjee, A.; Ren, D.; Vullum, P.-E.; Huh, J.; Fimland, B.-O.; Weman, H. GaAs/AlGaAs Nanowire Array Solar Cell Grown on Si with Ultrahigh Power-per-Weight Ratio. *ACS Photonics* **2021**, *8*, 2355–2366. [CrossRef]
94. Gibson, S.J.; van Kasteren, B.; Tekcan, B.; Cui, Y.; van Dam, D.; Haverkort, J.E.M.; Bakkers, E.P.A.M.; Reimer, M.E. Tapered InP Nanowire Arrays for Efficient Broadband High-Speed Single-Photon Detection. *Nat. Nanotechnol.* **2019**, *14*, 473–479. [CrossRef] [PubMed]
95. Zhu, Y.; Raj, V.; Li, Z.; Tan, H.H.; Jagadish, C.; Fu, L. Self-Powered InP Nanowire Photodetector for Single-Photon Level Detection at Room Temperature. *Adv. Mater.* **2021**, *33*, 2105729. [CrossRef] [PubMed]
96. Li, Z.; Azimi, Z.; Li, Z.; Yu, Y.; Huang, L.; Jin, W.; Tan, H.H.; Jagadish, C.; Wong-Leung, J.; Fu, L. InAs Nanowire Arrays for Room-Temperature Ultra-Broadband Infrared Photodetection. *Nanoscale* **2023**, *15*, 10033–10041. [CrossRef] [PubMed]
97. Mukherjee, A.; Ren, D.; Mosberg, A.B.; Vullum, P.-E.; van Helvoort, A.T.J.; Fimland, B.-O.; Weman, H. Origin of Leakage Currents and Nanowire-to-Nanowire Inhomogeneity in Radial p–i–n Junction GaAs Nanowire Array Solar Cells on Si. *ACS Appl. Nano Mater.* **2023**, *6*, 14103–14113. [CrossRef]
98. Hrachowina, L.; Chen, Y.; Barrigón, E.; Wallenberg, R.; Borgström, M.T. Realization of Axially Defined GaInP/InP/InAsP Triple-Junction Photovoltaic Nanowires for High-Performance Solar Cells. *Mater. Today Energy* **2022**, *27*, 101050. [CrossRef]
99. Espinet-Gonzalez, P.; Barrigón, E.; Otnes, G.; Vescovi, G.; Mann, C.; France, R.M.; Welch, A.J.; Hunt, M.S.; Walker, D.; Kelzenberg, M.D.; et al. Radiation Tolerant Nanowire Array Solar Cells. *ACS Nano* **2019**, *13*, 12860–12869. [CrossRef]
100. Chen, Y.; Pistol, M.-E.; Anttu, N. Design for Strong Absorption in a Nanowire Array Tandem Solar Cell. *Sci. Rep.* **2016**, *6*, 32349. [CrossRef]
101. Fast, J.; Aeberhard, U.; Bremner, S.P.; Linke, H. Hot-Carrier Optoelectronic Devices Based on Semiconductor Nanowires. *Appl. Phys. Rev.* **2021**, *8*, 021309. [CrossRef]